Computers in Biology and Medicine 114 (2019) 103436

Contents lists available at ScienceDirect

Computers in Biology and Medicine

journal homepage: http://www.elsevier.com/locate/compbiomed

Geometric determinants of local hemodynamics in severe carotid artery stenosis

Dara Azar [a,1], William M. Torres [a,b,1], Lindsey A. Davis [a,c], Taylor Shaw [c], John F. Eberth [a,c], Vijaya B. Kolachalama [d], Susan M. Lessner [a,c], Tarek Shazly [a,e,*]

[a] Biomedical Engineering Program, College of Engineering and Computing, University of South Carolina, Columbia, SC, USA
[b] Exponent, Inc, Philadelphia, PA, USA
[c] Department of Cell Biology and Anatomy, University of South Carolina School of Medicine, Columbia, SC, USA
[d] Section of Computational Biomedicine, Department of Medicine, Boston University School of Medicine, Boston, MA, USA
[e] Department of Mechanical Engineering, College of Engineering and Computing, University of South Carolina, Columbia, SC, USA

ARTICLE INFO

Keywords:
Carotid endarterectomy
Carotid stenosis
Computational fluid dynamics
Plaque geometry
Prediction models

ABSTRACT

In cases of severe carotid artery stenosis (CAS), carotid endarterectomy (CEA) is performed to recover lumen patency and alleviate stroke risk. Under current guidelines, the decision to surgically intervene relies primarily on the percent loss of native arterial lumen diameter within the stenotic region (i.e. the degree of stenosis). An underlying premise is that the degree of stenosis modulates flow-induced wall shear stress elevations at the lesion site, and thus indicates plaque rupture potential and stroke risk. Here, we conduct a retrospective study on pre-CEA computed tomography angiography (CTA) images from 50 patients with severe internal CAS (>60% stenosis) to better understand the influence of plaque and local vessel geometry on local hemodynamics, with geometrical descriptors that extend beyond the degree of stenosis. We first processed CTA images to define a set of multipoint geometric metrics characterizing the stenosed region, and next performed computational fluid dynamics simulations to quantify local wall shear stress and associated hemodynamic metrics. Correlation and regression analyses were used to relate obtained geometric and hemodynamic metrics, with inclusion of patient sub-classification based on the degree of stenosis. Our results suggest that in the context of severe CAS, prediction of shear stress-based metrics can be enhanced by consideration of readily available, multipoint geometric metrics in addition to the degree of stenosis.

1. Introduction

Carotid artery interventions, such as carotid endarterectomy (CEA) and carotid artery stenting, have been used for over half a century to reduce stroke risk in patients presenting with severe carotid artery stenosis (CAS). However, these interventions carry an aggregate complication rate of 4.5%–7.0%, with potential negative outcomes including myocardial infarction, pulmonary embolism, and post-operative stroke [9,34,35]. Clinical observations and experimental studies have demonstrated the importance of plaque geometry on local hemodynamics and embolic potential, motivating consideration of the degree of vessel stenosis in clinical decision making [3,21,25,32,39]. Current guidelines for CEA from most major international bodies recommend intervention for neurologically symptomatic CAS with $\geq$ 70% diameter reduction in the internal carotid artery (ICA), while others use a threshold of $\geq$ 50% diameter reduction [18,33]. Clinical guidelines recommend that in these cases, surgery is performed within two weeks of the onset of neurological symptoms [37]. Existing guidelines for neurologically asymptomatic cases are less uniform, but clinical decision-making still depends mainly on the maximum degree of stenosis [33,37]. In addition to the degree of stenosis, higher fidelity geometric details of the atherosclerotic plaque and parent vessel are accessible via clinical imaging including computed tomography angiography (CTA), and have been shown to significantly impact the local blood flow field and plaque mechanics [7,10,20,22]. For instance, an increase in lesion axial length is inversely related to axial plaque stress in severely stenotic cases ($\geq$60%), thus suggesting extended lesions have relatively diminished embolic potential [7]. Plaque asymmetry in the stenosed region has also been shown to

* Corresponding author. Department of Mechanical Engineering, College of Engineering and Computing, University of South Carolina, Columbia, SC, USA.
E-mail address: shazly@cec.sc.edu (T. Shazly).
[1] Indicates equal contribution.

https://doi.org/10.1016/j.compbiomed.2019.103436
Received 5 July 2019; Received in revised form 3 September 2019; Accepted 4 September 2019
Available online 5 September 2019

impact local wall shear stress magnitudes and flow recirculation patterns [10,38]. Other studies have found correlation between vessel tortuosity and flow-dependent pressure gradients, with a co-dependence on the degree of stenosis [27]. In a study that examined both degree of stenosis and plaque eccentricity, these factors exhibited a strong interactive effect on the wall shear stress distribution [19]. In these and other studies, finite element-based computational fluid dynamics (CFD) models were used to interrelate plaque geometry and local hemodynamics [2,3,28,46].

Clinical integration of CFD models requires a noninvasive, image-based assessment of plaque and vessel geometry and estimation of inlet/outlet blood velocities/pressures in a control volume encompassing the diseased vasculature. CFD solutions provide three-dimensional transient velocity/pressure fields and enable quantification of multiple hemodynamic metrics. These metrics include: flow-induced wall shear stress (WSS) – the tangential friction force on the endothelial or plaque surface; oscillatory shear index (OSI) – the temporal fluctuation of the WSS; and relative residence time (RRT) – the relative dynamic measure of local nonadherent particles within the flow field. These metrics have been linked to plaque accumulation, remodeling, and rupture risk [6,40].

The goal of the present study was to process pre-CEA CTA images to define and quantify multipoint descriptors of lesion geometry, and then build CFD models to compute hemodynamic metrics at the lesion site. Our hypothesis is that multiple metrics of lesion geometry, including but not limited to the degree of stenosis, will interactively modulate local hemodynamics in stenotic carotid arteries.

2. Methods

2.1. Patient-specific data acquisition

Fifty de-identified CTA images in DICOM format were obtained from patients with highly stenotic ICAs evaluated for CEA (Greenville Health System, Greenville, SC). According to the North American Symptomatic Carotid Endarterectomy Trial (NASCET) criteria, all cases were at a high risk of stroke with the degree of stenosis ranging from 67.4% to 99.1%. Handling and processing of patient images were performed in accordance with institutional ethics committee guidelines. All patients gave informed consent for use of their clinical imaging studies under IRB protocol (Pro00027940).

2.2. Geometry reconstruction and analysis

2.2.1. Reconstruction of patient-specific geometries

A semi-automated approach was developed to efficiently reconstruct the 3D arterial lumen and identify patient-specific geometric variables of the plaque and local vasculature (elaborated upon in subsequent sections). This semi-automated process yielded reproducible assessments independent of operator variability while minimizing time and resource consumption. The CTA volume is represented in a series of 2D images with a known distance between each image. A segmentation protocol was established using the Vascular Modeling Toolkit (VMTK; www.vmtk.org), an open-source pre-processing resource, to identify the boundaries of the arterial lumen for each slice of the scan using the distinct density-dependent voxel intensities between the angiography contrast dye and the plaque/arterial wall. The underlying algorithm in this automated process is based on an identification of centerlines and a robust decomposition of the bifurcation into its constituent branches, followed by mapping the surface of each of the branches onto the parametric plane [1]. After manual selection of a seed point and definition of bounds, the boundaries of the arterial lumen were detected and smoothing algorithms were applied to remove fine-scale irregularities from the reconstructed surface. Finally, a non-uniform rational b-spline was then fit to the surface to facilitate domain discretization for CFD analysis (Fig. 1A).

Reconstructed domains were imported into the ANSYS ICEM-CFD meshing software and fit with a linear tetrahedral surface mesh using a robust octree formulation [8,12,17]. After smoothing this mesh to increase the quality of the individual elements, a tetrahedral volume mesh was generated using a Delauney formulation [38,46]. Finally, the arterial wall was fit with a triple layer of post-inflation hexahedral prism elements to allow for a more accurate capture of the hemodynamics in the boundary layer.

2.2.2. Calculation of geometric variables

A MATLAB code was developed to extract the centerline along the vessel geometry and the cross-sectional area function ($A(x)$) at every point along the centerline path [1]. $A(x)$ was computed based on normal cross-sections of maximal inscribed spheres along the centerline. Geometric variables (described below) were calculated from $A(x)$ center-point coordinates and the associated function value. The region of interest (ROI) for geometric variable calculation was a 5 mm radius sphere with a center-point coincident with the maximal degree of stenosis (S_{max}) (Fig. 1B). The employed ROI sphere radius (5 mm) was motivated by typical lesion length (along the centerline) across the entire study cohort. Shear stress and related metrics (discussed in below sections) were temporally- and spatially-averaged within the ROI to minimize response variable sensitivity to model discretization.

A set of nine geometric variables were extracted from the reconstructed geometries to describe the complex geometry of the ROI. Degree of stenosis, S, is the ratio between the minimal lumen area within the ROI and the proximal lumen area of the non-diseased section of the common carotid artery. For subsequent analyses, cases were subclassified based on the degree of stenosis ($0.67 < S < 0.80$, $0.80 \leq S < 0.90$ and $0.90 \leq S < 1.00$; where $S \times 100$ corresponds to the percentage of stenosis). Proximal tortuosity, τ_P, and distal tortuosity, τ_D,

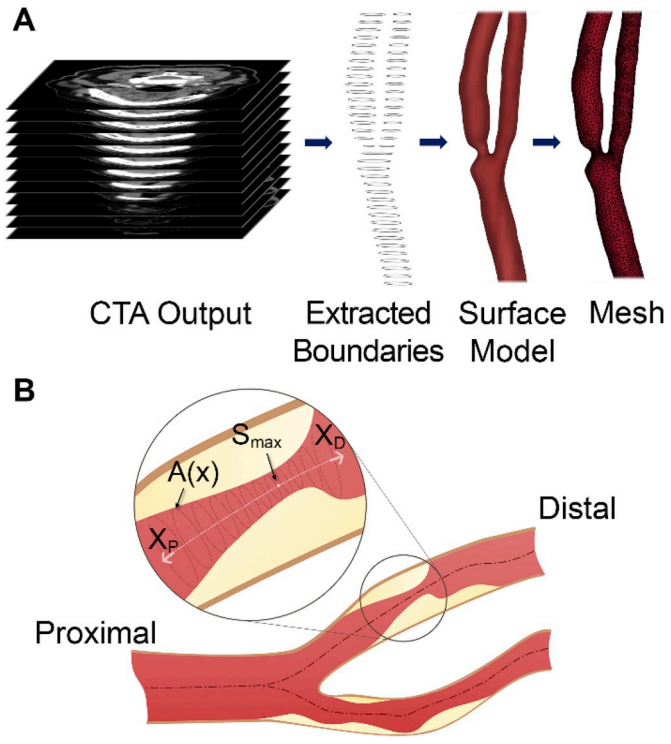

Fig. 1. Carotid artery reconstruction and the 2D illustration of stenotic carotid artery. (A) Carotid artery reconstruction steps; CTA imaging output shown by a stack of 2D images of a representative carotid artery segment, extracted boundaries to define the surface of the arterial lumen, surface model and the linear tetrahedral volumetric mesh. (B) The maximal stenosis S_{max} and cross-sectional area A(x) are depicted. X_D and X_P specific center-point locations in the distal and proximal directions, respectively.

are the ratios of the centerline path length divided by the point-to-point distances from S_{max} to the proximal and distal ends of the ROI, respectively. Proximal luminal concavity, C_P, and distal luminal concavity, C_D, are the absolute values of the second derivative of $A(x)$ with respect to proximal/distal locations (x). $A(x)$ is a quadratic function that returns the lumen area at the position x defined with respect to the location of S_{max}. Proximal area-averaged slope, $\overline{m}_P$, and distal area-averaged slope, $\overline{m}_D$, are the integrals of the first derivative of $A(x)$ with respect to distance divided by the area function in either proximal and distal sides of the S_{max}, respectively. Stenosis-to-proximal-end slope, m_P, and distal-end-to-stenosis slope, m_D, are the absolute values of the change in lumen area over end-to-end distance (Table 1).

2.3. CFD model construction

CFD models were developed with a finite volume-based Navier-Stokes solver (ANSYS-Fluent v. 17.2), and each model was run over three cardiac cycles under an assumption of laminar flow [26,29]. The results presented here refer to averages obtained over the third cardiac cycle in order to minimize the influence of initial flow conditions. The blood was characterized as an incompressible non-Newtonian Carreau fluid ($\eta_0 = 0.25$ Pa s; $\eta_\infty = 0.0035$ Pa s; $\lambda = 25$; $n = 0.25$) with a constant density of 1060 kg/m^3 and zero-slip boundary conditions were applied to the rigid arterial walls [29]. A previously acquired carotid artery velocity profile attained from a healthy human male subject was converted to a continuous function using a Fourier transform and then used as an inlet velocity boundary condition on the proximal segment of the common carotid artery (CCA) [14,31,36,48]. A fully developed velocity profile was established within 2 cm downstream of the inlet across all cases. In accordance with prior studies on highly stenoses carotid arteries, uniform pressures of 70 mmHg and 90 mmHg were prescribed to the internal and external carotid artery outlets, respectively [45]. A mesh-independent solution was identified in a subset of cases (5) as the lowest mesh density for which subsequently increasing density (>30% increase in total number of elements) did not significantly alter the computed peak WSS value (<1% change). Based on these studies, a minimum of 100,000 elements spanning the 8 cm length of the reconstructed carotid bifurcation was used in all models.

Table 1
Definition of geometric variables with respective formulae.

Geometric variables	Definition
Degree of stenosis; S	$= 1 - \frac{minimum\ A(x)}{maximum\ A(x)}$
Proximal tortuosity; τ_P	$= \frac{Length}{Distance}$ between the vessel centerline at the proximal end of the region of interest and S_{max}
Distal tortuosity; τ_D	$= \frac{Length}{Distance}$ between the vessel centerline at the distal end of the region of interest and S_{max}
Proximal luminal concavity; C_P	$= \left\lvert \frac{d^2A}{dx^2_{Prox/Distal}} \right\rvert$, where A is a quadratic function of distance on proximal side; $A(x) = ax^2 + bx + c$.
Distal luminal concavity; C_D	$= \left\lvert \frac{d^2A}{dx^2_{Prox/Distal}} \right\rvert$, where A is a quadratic function of distance on distal side; $A(x) = ax^2 + bx + c$.
Proximal area-averaged slope; $\overline{m}_P$	$= \int_0^{X_{Prox/Distal}} \frac{\frac{dA}{dx_{Prox/Distal}}}{A} dx$, where A is a quadratic function of distance on proximal side; $A(x) = ax^2 + bx + c$.
Distal area-averaged slope; $\overline{m}_D$	$= \int_0^{X_{Prox/Distal}} \frac{\frac{dA}{dx_{Prox/Distal}}}{A} dx$, where A is a quadratic function of distance on distal side; $A(x) = ax^2 + bx + c$.
Stenosis-to-proximal-end slope; m_P	$= \left\lvert \frac{\Delta A}{\Delta X_{Prox/Distal}} \right\rvert$, where ΔA is the area change over length on proximal side of the region of interest.
Distal-end-to-stenosis slope; m_D	$= \left\lvert \frac{\Delta A}{\Delta X_{Prox/Distal}} \right\rvert$, where ΔA is the area change over length on distal side of the region of interest.

2.4. Post-processing

2.4.1. Hemodynamic response variables

To calculate time-averaged wall shear stress (TAWSS), the instantaneous WSS was calculated and then averaged spatially/temporally across all elements in the ROI over the third cardiac cycle:

$$\mathrm{TAWSS} = \frac{1}{T}\int_0^T |WSS| dt \tag{1}$$

Mean oscillatory shear index (OSI) is a dimensionless parameter ranging from 0 to 0.5 that is defined based on the temporal fluctuation of WSS and averaged over the ROI, as:

$$\mathrm{OSI} = 0.5\left[1 - \frac{\left|\int_0^T WSS\ dt\right|}{\int_0^T |WSS| dt}\right] \tag{2}$$

where T is the elapsed time and WSS is the magnitude at each individual node. Mean relative residence time (RRT) considers both the averaged WSS and mean OSI:

$$\mathrm{RRT} = \frac{1}{\mathrm{TAWSS}(1 - 2\ \mathrm{OSI})} = \frac{1}{\left|\int_0^T WSS\ dt\right|} \tag{3}$$

with values reported in Pa^{-1}. RRT reflects the residence time of blood in contact with or near the endothelium and is considered an important factor in plaque genesis [29].

2.4.2. Statistical analyses

Data were analyzed using MATLAB to identify correlations between geometric and hemodynamic variables, with Spearman correlation used to quantify correlation strength and significance. Correlation analyses were carried for all cases together (general approach) or a piecewise approach that was based on a sub-classification of cases via degree of stenosis ($0.67 < S < 0.80$, $0.80 \le S < 0.90$ and $0.90 \le S < 1.00$). Geometrical variables with statistically significant correlation to a given CFD hemodynamic variable were then used to develop predictive regression models that consider the former as input and the latter as output. Backward stepwise multiple linear regression was performed for model parameter identification, with inclusion of variable interactions only if model R^2 was increased by > 0.05 due to the inclusion. Regression models were developed based on either the entire sample set (general regression) or over the defined sub-classification ranges (piecewise regression). Of the 50 CTA images, 45 were used for regression model parameter identification, and 5 were reserved for evaluating the predictive capability of the regression models by comparing predicted values of hemodynamic response variables against obtained CFD results.

3. Results

CTA-based vessel geometric models were used to extract geometric variables (9 per case) using the aforementioned semi-automated approach. Geometric models were also used in CFD simulations that compute local hemodynamic response variables derived from WSS (3 per case). Descriptive statistics for geometrical variables and CFD-based hemodynamic variables are shown in Fig. 2. Three representative cases from each sub-classifications of the degree of stenosis are shown along with the distribution of hemodynamic variables relative to the degree of stenosis (Fig. 3).

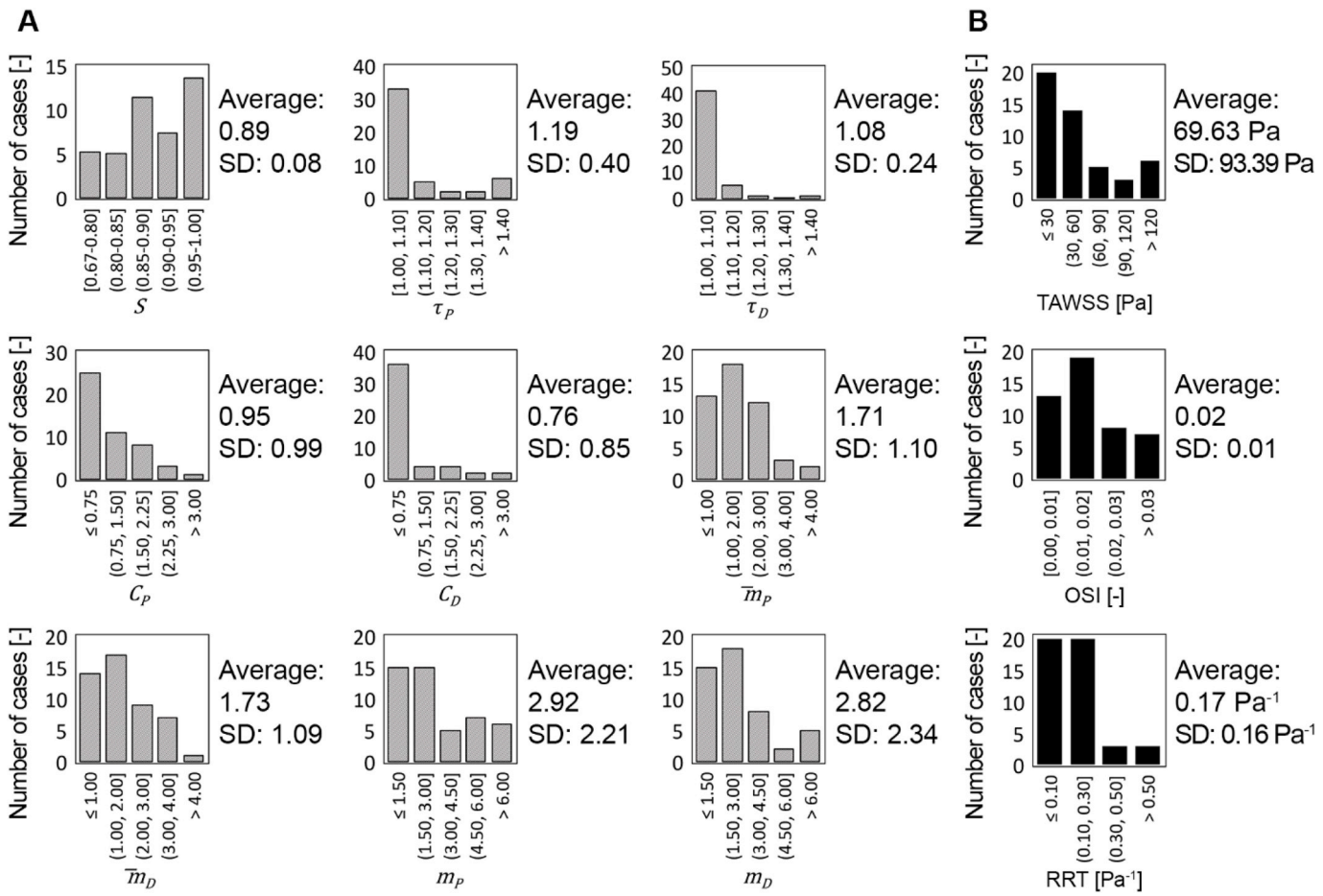

Fig. 2. Descriptive statistics of CTA-based geometric variables and results obtained from CFD simulations. (A) Each bar represents a range of values. The length of each bar denotes the number of each range for each of the geometric variables; Degree of Stenosis; S, Proximal Tortuosity; τ_P , Distal Tortuosity; τ_D , Proximal Luminal Concavity; C_P , Distal Luminal Concavity; C_D, Proximal Area-Averaged Slope; $\overline{m}_P$, Distal Area-Averaged Slope; $\overline{m}_D$, Stenosis-to-Proximal-end Slope; m_P and Distal-end-to-Stenosis Slope; m_D. (B) - output variables calculated from CFD simulations; TAWSS, OSI and RRT.

3.1. Simulation results and correlation: TAWSS

Computational simulations qualitatively show an increase in TAWSS magnitudes with increasing degree of stenosis, with clearly nonuniform stress distributions both proximal and distal to the bifurcation point (Fig. 3A). Within these cases of severe CAS, TAWSS was generally elevated with increasing degree of stenosis. However, an exponential regression model was statistically insignificant when applied across all cases (R [2] = 0.52; p = 0.14), motivating consideration of additional geometric variables to predict shear stress and related metrics. When sub-classified based on the degree of stenosis, TAWSS is relatively more sensitive to increased stenosis in the severe cases ($0.90 \leq S < 1.00$); with averaged values of 17.81 ± 16.05 Pa, 29.74 ± 15.95 Pa and 118.72 ± 117.71 Pa for $0.67 < S < 0.80$, $0.80 \leq S < 0.90$ and $0.90 \leq S < 1.00$, respectively (Fig. 3A). While a general correlation analysis revealed a positive correlation between TAWSS and the degree of stenosis, as well as both proximal and distal area-averaged slopes, the significance of these factors was not fully maintained throughout piecewise correlation analysis (Fig. 4). Most notably, no correlation between TAWSS and the degree of stenosis was observed in the intermediate stenosis subclassification ($0.80 \leq S < 0.90$).

3.2. Simulation results and correlation: OSI and RRT

Representative colorimetric plots of OSI and RRT underscore the inherent relation between these flow field metrics, with obvious coincidence of vessel regions experiencing locally elevated values (Fig. 3B and C). There was no general correlation ($p < 0.15$) between the area-averaged mean OSI and the degree of stenosis, and only sporadic correlation when sub-classifications were considered (Fig. 4). Using the general correlation analysis, no statistically significant relationship was found between OSI and any of the defined geometric variables. For the OSI piecewise correlation analyses, there is at least one geometric variable with stronger correlation as compared to degree of stenosis in each subclassification range. Area-averaged mean RRT exhibits a consistent negative correlation to the degree of stenosis, with the strongest relation in the least stenosed vessels ($0.67 < S < 0.80$) (Fig. 4).

3.3. Regression models

Multiple linear regression models were generated using the defined geometric variables that correlated with CFD hemodynamic variables ($p < 0.1$), as well as potential interactive effects among these geometric variables. For each of the hemodynamic variables, the following general and piecewise regression models were obtained:

TAWSS.

General:

$$\textit{Mean TAWSS}\ [\text{Pa}] = 261.44 - 274.7 \times S - 488.04 \times \overline{m}_D + 564.64 \times S \times \overline{m}_D, \quad p < 0.001$$

Piecewise:

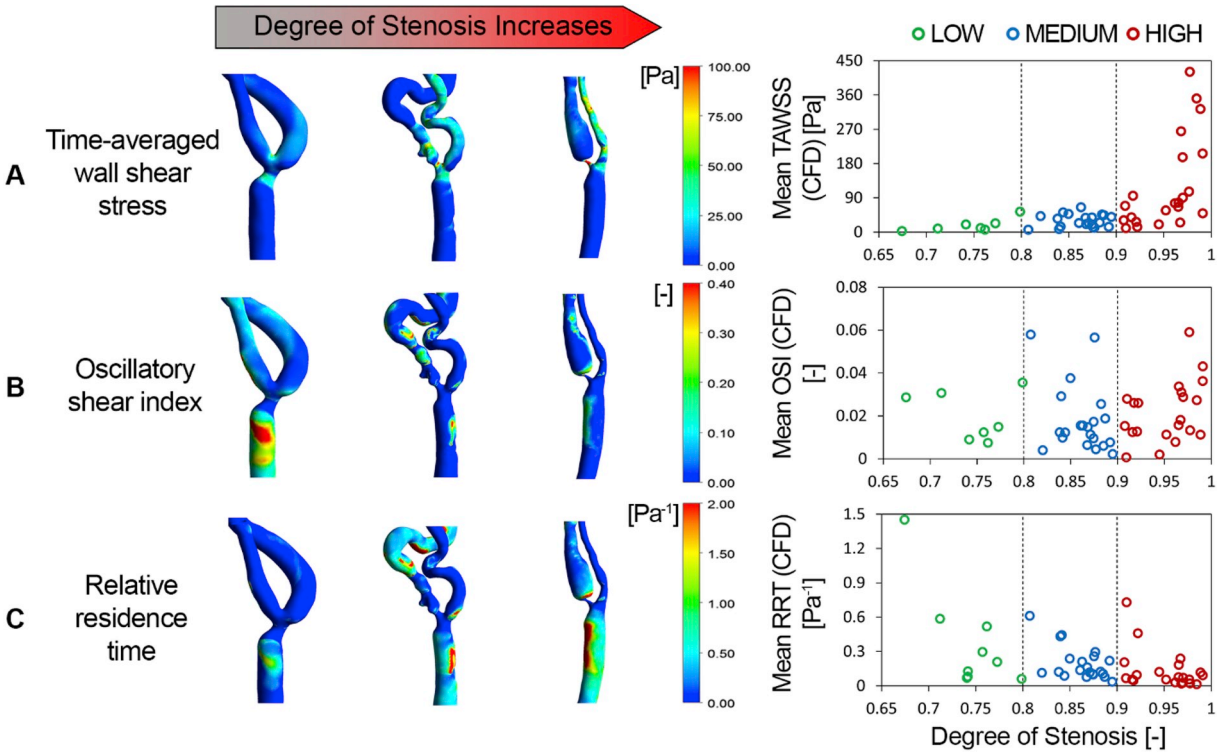

Fig. 3. 3D mapping of results from CFD simulations for a representative sample of reconstructed geometries selected from each of the three ranges of stenotic severity ($0.67 < S < 0.80$, $0.80 \leq S < 0.90$ and $0.90 \leq S < 1.00$) and the distribution of hemodynamic variables with respect to the degree of stenosis for all samples. Stenosis severity ranges from $0.67 < S < 1$ and datapoints are labeled with different colors indicating the severity category (Green: $0.67 < S < 0.80$, Blue: $0.80 \leq S < 0.90$ and Red: $0.90 \leq S < 1.00$). (A) 3D mapping of TAWSS for three representative cases and distribution of TAWSS with respect to degree of stenosis. (B) 3D mapping of OSI for three representative cases and distribution of OSI with respect to degree of stenosis. (C) 3D mapping of RRT for three representative cases and distribution of RRT with respect to degree of stenosis. (For interpretation of the references to color in this figure legend, the reader is referred to the Web version of this article.)

$$Mean\ \ TAWSS\ \left[\mathrm{Pa}\right] = \begin{cases} 17.94 - 3.471 \times \overline{m}_D - 19.30 \times m_D + 20.578 \times \overline{m}_D \times m_D & 0.67 < S < 0.80, \quad p = 0.075 \\ 8.8104 + 17.278 \times \overline{m}_P & 0.80 \leq S < 0.90, \quad p = 0.035 \\ -1754.8 + 1856.9 \times S + 49.766 \times \overline{m}_D & 0.90 \leq S < 1.00, \quad p = 0.002 \end{cases}$$

OSI.
General: —
Piecewise:

Piecewise:

The descriptive and predictive capabilities of identified regression models were evaluated by comparing model- and CFD-derived values of hemodynamic response variables (Fig. 5). While no significant general regression model was obtained for OSI, piecewise regression resulted in significant descriptive and predictive models (Fig. 5B). Piecewise as opposed to general regression modeling resulted in a substantial improvement in both the descriptive and predictive capabilities with respect to TAWSS and RRT (Fig. 5A and C).

$$Mean\ OSI\ \left[-\right] = \begin{cases} 0.009 + 0.017 \times C_D & 0.67 < S < 0.80, \quad p = 0.066 \\ 0.065 - 0.04 \times \overline{m}_D - 0.018 \times m_D - 0.013\, m_D \times \overline{m}_D & 0.80 \leq S < 0.90, \quad p = 0.001 \\ -0.235 + 0.278 \times S + 0.159 \times \overline{m}_P - 0.008 \times \overline{m}_D - 0.178\, S \times \overline{m}_P + 0.006 \times \overline{m}_P \times \overline{m}_D & \\ 0.90 \leq S < 1.00, \quad p = 0.010 & \end{cases}$$

RRT.
General:

$$Mean\ RRT\ \left[\mathrm{Pa}^{-1}\right] =$$

$$0.355 - 0.1437 \times S + 0.609 \times C_D - 0.504 \times \overline{m}_D + 0.265 \times m_P - 0.63 \times S \times C_D + 0.493 \times S \times \overline{m}_D - 0.341 \times S \times m_P - 0.068 \times C_D \times \overline{m}_D + 0.0566 \times C_D \times m_P + 0.0184 \times \overline{m}_D \times m_P, \qquad p < 0.001$$

A All

Geometrical Variables	Mean TAWSS [Pa]	Mean OSI [-]	Mean RRT [Pa^{-1}]
Degree of Stenosis; S	0.67**	0.16	-0.57**
Proximal Tortuosity; τ_P	-0.05	0.16	0.07
Distal Tortuosity; τ_D	0.16	0.08	-0.36
Proximal Luminal Concavity; C_P	-0.14	0.09	0.31
Distal Luminal Concavity; C_D	-0.09	0.26	0.25*
Proximal Area-Averaged Slope; $\overline{m}_P$	0.44**	0.22	-0.23
Distal Area-Averaged Slope; $\overline{m}_D$	0.56**	0.04	-0.42**
Stenosis-to-Proximal-end Slope; m_P	-0.09	0.08	0.24*
Distal-end-to-Stenosis Slope; m_D	0.00	-0.08	-0.07

B 0.67 < S < 0.80

Geometrical Variables	Mean TAWSS [Pa]	Mean OSI [-]	Mean RRT [Pa^{-1}]
Degree of Stenosis; S	0.75*	-0.04	-0.75*
Proximal Tortuosity; τ_P	-0.43	0.39	0.43
Distal Tortuosity; τ_D	-0.46	-0.11	0.29
Proximal Luminal Concavity; C_P	-0.53	-0.11	0.86**
Distal Luminal Concavity; C_D	0.14	0.82**	-0.20
Proximal Area-Averaged Slope; $\overline{m}_P$	-0.55	0.11	0.79**
Distal Area-Averaged Slope; $\overline{m}_D$	0.82**	0.46	-0.68*
Stenosis-to-Proximal-end Slope; m_P	-0.61	-0.25	0.82**
Distal-end-to-Stenosis Slope; m_D	0.79**	0.39	-0.50

C 0.80 ≤ S < 0.90

Geometrical Variables	Mean TAWSS [Pa]	Mean OSI [-]	Mean RRT [Pa^{-1}]
Degree of Stenosis; S	0.07	-0.26	-0.37*
Proximal Tortuosity; τ_P	0.00	0.28	-0.01
Distal Tortuosity; τ_D	-0.09	-0.12	-0.35
Proximal Luminal Concavity; C_P	0.43	0.04	0.07
Distal Luminal Concavity; C_D	-0.40	0.20	0.41*
Proximal Area-Averaged Slope; $\overline{m}_P$	0.65**	0.05	0.17
Distal Area-Averaged Slope; $\overline{m}_D$	0.11	-0.45**	-0.27
Stenosis-to-Proximal-end Slope; m_P	0.03	0.10	0.42*
Distal-end-to-Stenosis Slope; m_D	0.04	-0.41*	-0.26

D 0.90 ≤ S < 1.00

Geometrical Variables	Mean TAWSS [Pa]	Mean OSI [-]	Mean RRT [Pa^{-1}]
Degree of Stenosis; S	0.65**	0.46**	-0.35*
Proximal Tortuosity; τ_P	-0.27	-0.12	0.27
Distal Tortuosity; τ_D	0.24	0.23	-0.29
Proximal Luminal Concavity; C_P	-0.09	0.19	0.45**
Distal Luminal Concavity; C_D	-0.26	-0.04	0.22
Proximal Area-Averaged Slope; $\overline{m}_P$	0.36	0.41*	-0.13
Distal Area-Averaged Slope; $\overline{m}_D$	0.61**	0.47**	-0.23
Stenosis-to-Proximal-end Slope; m_P	-0.37	0.18	0.39*
Distal-end-to-Stenosis Slope; m_D	-0.34	0.13	0.32

Fig. 4. Spearman correlation analysis results for ρ demonstrating the strength of the association between hemodynamic and geometric variables. (A) Spearman correlation coefficient and statistical significance assessment using the general approach and including all samples. (B-D) – using the piecewise approach with $0.67 < S < 0.80$, $0.80 \leq S < 0.90$ and $0.90 \leq S < 1.00$, respectively. $\rho > 0$ and $\rho < 0$ values are shaded with shades of red and blue, respectively. darker shades indicate greater magnitudes of ρ values. (* indicates p-value<0.1 and ** indicates p-value<0.05). (For interpretation of the references to color in this figure legend, the reader is referred to the Web version of this article.)

$$Mean\ RRT\ \left[\mathrm{Pa}^{-1}\right] = \begin{cases} 9.821 - 10.604 \times S - 10.916 \times C_P - 0.435 \times \overline{m}_P + 12.414 \times C_P \times \overline{m}_P & \\ \quad 0.67 < S < 0.80, & p = 0.011 \\ -3.93 + 4.64 \times S + 4.665 \times C_D + 1 \times m_P - 5.312 \times S \times C_D - 1.138 \times S \times m_P & \\ \quad 0.80 \leq S < 0.90, & p < 0.001 \\ 1.106 + 1.199 \times S + 1.064 \times m_P - 1.095 \times S \times m_P & 0.90 \leq S < 1.00, \quad p = 0.018 \end{cases}$$

4. Discussion

The present study involves presurgical CTA scans from 50 patients with sufficient carotid artery stenosis to meet the current NASCET guidelines for the recommendation of open surgery intervention (i.e. carotid endarterectomy). These guidelines, although are the current gold standard for surgical decision making, inherently rely on one geometric parameter determined at one axial plaque location [15]. Several experimental and computational studies have elucidated the importance of other geometrical attributes of the plaque on flow-induced wall shear stress, flow reversal and the progression of the stenotic occlusion [7,10,44]. To that end, the primary goal of this study was to identify a set of novel local geometric variables that can collectively predict local wall shear stress and related hemodynamic indicators of risk in highly stenotic carotid arteries. Although risk assessment in CAS is highly multifactorial, this work focuses on predicting local shear stress levels based on patient-specific geometry.

Regions with complex geometries are susceptible to focal complications arising from low WSS, exemplified by the prevalence of carotid atheroma in the vicinity of the carotid bifurcation [11,47]. Conversely, moderately elevated WSS (~30 Pa) can promote the formation of lumen thrombus and severely elevated WSS (over 40 Pa) can cause local endothelial injury and denudation [16]. Several previous studies have examined trends in the TAWSS in severely stenotic cases; Li et al. reported TAWSS as high as 73 Pa located distal to the point of maximal stenosis in a patient-specific model [26]. A similar observation was made by Su et al., noting elevated TAWSS (79 Pa) with 90% stenosis, compared to baseline values that were less than 12 Pa [42]. As reported in the literature and observed this study, stenosis generally elevates TAWSS but does so in a complex manner that is suggestive of interactive effects with other geometric characteristics [7,44].

Spatial and temporal fluctuations of the WSS vector are quantified by the mean OSI and RRT. Higher degrees of stenotic occlusion (>50–60%) are associated with a sharp increase of OSI and RRT [29]. It was shown previously that in an idealized geometry, an increase in stenosis results in larger downstream vortices, and as a result higher magnitudes of OSI become more prominent farther from the maximum stenosis [29,44]. We observed a reduction in OSI local to the lesion which our results find to be independent of the local geometry [13,24]. OSI, however, does show a positive association with stenosis as occlusion progresses and demonstrates correlations with parameters other than stenosis at different stages of the pathology (i.e. three subcategories of stenotic

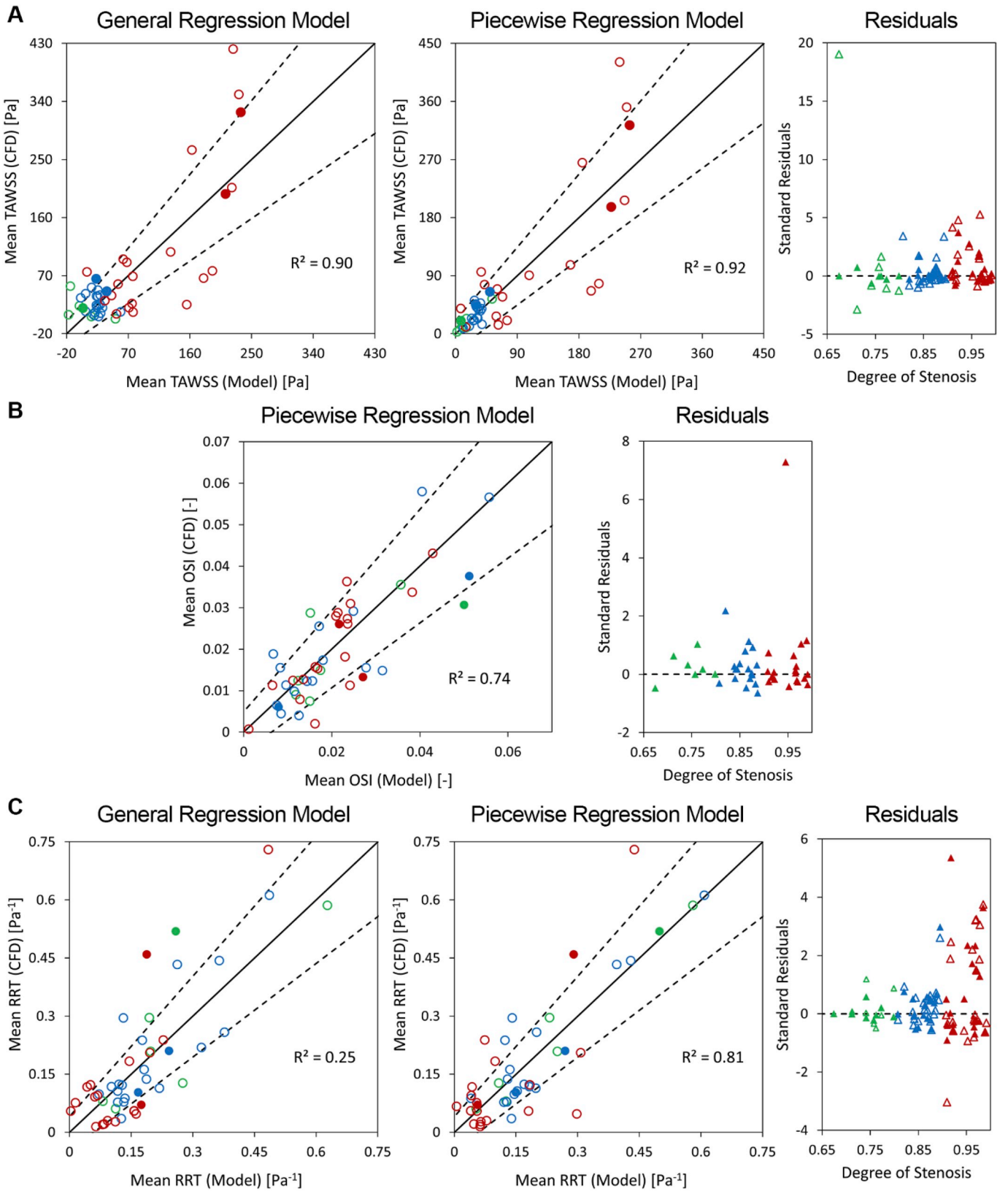

(caption on next page)

Fig. 5. Relationship between hemodynamic variables obtained from CFD results with respect to the regression models and respective residuals. (A) Distribution of the TAWSS from CFD and regression models (general and piecewise) obtained using 45 cases. Filled data points show values predicted by the model that were not used in development of the model (5 cases). (Right) Distribution of residuals with respect to the degree of stenosis for all samples using general regression and piecewise regression model; filled data points indicate results from the piecewise model. (General model average residual and standard deviation: 0.86 and 3.10, respectively. Piecewise model average residual and standard deviation: 0.28 and 0.90, respectively). (B) Distribution of the OSI from CFD and piecewise regression model obtained using 45 cases. Filled data points show values predicted by the model that were not used in development of the model (5 cases). (Right) Distribution of residuals with respect to the degree of stenosis for all samples using piecewise regression model. (Average residual and standard deviation: 0.35 and 1.18, respectively). (C) Distribution of the RRT from CFD and regression models (general and piecewise) obtained using 45 cases. Filled data points show values predicted by the model that were not used in development of the model (5 cases). (Right) Distribution of residuals with respect to the degree of stenosis for all samples using general regression and piecewise regression model; filled data points indicate results from the piecewise model. (General model average residual and standard deviation: 0.46 and 1.27, respectively. Piecewise model average residual and standard deviation: 0.43 and 1.18, respectively). For all (A), (B) and (C), datapoints are labeled with different colors (Green, Blue and Red; from low to high) indicating their associated stenosis severity category, and dotted lines represent 95% confidence intervals. (For interpretation of the references to color in this figure legend, the reader is referred to the Web version of this article.)

severity). Furthermore, our qualitative examinations confirmed an increase of OSI distal and proximal to the lesion site, areas where flow reversal is predominant [13,30].

For RRT, it was shown that the degree of stenosis has a strong negative association with the RRT, regardless of what sample population was considered. Strong negative correlation between the degree of stenosis and the mean RRT in the ROI can be explained with the increased pressure gradient induced by the pathology that will result in lower residence time while WSS values are maximal [13,29]. An interesting outcome of this study is that all correlating proximal characteristics showed a positive relation with the RRT, and almost all distal parameters a negative relation. Among all geometric variables that demonstrated correlation within sub-classifications, the positive correlation between m_P and the mean RRT remained consistent and thus is strong candidate variable to predict RRT directly from CTA images.

4.1. Limitations

While our study incorporated a total of 50 cases and yielded multiple significant predictors of local hemodynamic variables, identified regression models may not be relevant to non-severe cases. In these models, vessel walls are assumed rigid; results might differ in models with deformable vessel walls and when fluid-structure interactions are accounted for. Furthermore, CFD models were built using patient-specific geometries, but representative flow field boundary conditions were applied uniformly across all cases. It is well acknowledged that the application of an inlet flow waveform acquired from a healthy patient diminishes the direct translational relevance of obtained results; however, uniform boundary conditions (among cases) were selected to facilitate isolation of geometric determinants of local wall shear stress. Additionally, all CFD models in this study were generated under the laminar flow assumption. While previous studies suggest a likely transition to turbulent flow in the case of highly stenotic carotid arteries, we only considered laminar flow [4,22,41,43]. Future iterations of our work will consider new segmentation methods in which flux-based higher order tensor is utilized for an improved modeling accuracy at branching points [5]. Finally, our computational models must be validated in future studies via comparing predictions to results acquired from four-dimensional flow magnetic resonance imaging (MRI) and reference CFD analysis results [23].

5. Conclusion

Our study is based on the definition and quantification of a novel set of local geometric variables which extended beyond the degree of stenosis. Computational results predict that key geometric variables, in addition to the degree of stenosis, significantly modulate local wall shear stress (and related metrics) in the context of severe CAS. Moreover, piece-wise multiple linear regression modeling suggests that different sets of geometric variables (which include the degree of stenosis) are determinants of wall shear stress across case subclassifications based solely on the degree of stenosis. We expect that different sets of geometric determinants would manifest under lower degrees of stenosis, which could be identified in CFD-based analyses and potentially influence surgical decision making in the context of CEA.

Sources of funding

This research was supported by the NIH INBRE Grant for South Carolina (P20GM103499), NSF Grant (CMMI-1760906) and the NIH/NIBIB (1R03 EB019663).

Disclosures

None.

Conflicts of interest

None Declared.

Acknowledgements

None.

References

[1] L. Antiga, D.A. Steinman, Robust and objective decomposition and mapping of bifurcating vessels, IEEE Trans. Med. Imaging 23 (2004) 704–713.
[2] H. Asgharzadeh, H. Asadi, H. Meng, I. Borazjani, A non-dimensional parameter for classification of the flow in intracranial aneurysms. II. Patient-specific geometries, Phys. Fluids 31 (2019) 031905.
[3] D. Azar, D. Ohadi, A. Rachev, J.F. Eberth, M.J. Uline, T. Shazly, Mechanical and geometrical determinants of wall stress in abdominal aortic aneurysms : a computational study, PLoS One 1–15 (2018). https://doi.org/10.1371/journal.pone.0192032.
[4] J. Banks, N.W. Bressloff, Turbulence modeling in three-dimensional stenosed arterial bifurcations, J. Biomech. Eng. 129 (2007) 40.
[5] S. Cetin, G. Unal, A higher-order tensor vessel tractography for segmentation of vascular structures, IEEE Trans. Med. Imaging 34 (2015) 2172–2185.
[6] Y. Chen, P. Zhang, X. Deng, Y. Fan, Y. Xing, N. Xing, Improvement of hemodynamic performance using novel helical flow vena cava filter design, Sci. Rep. 7 (2017) 40724.
[7] G. Choi, J.M. Lee, H.-J. Kim, J.-B. Park, S. Sankaran, H. Otake, J.-H. Doh, C.-W. Nam, E.-S. Shin, C.A. Taylor, B.-K. Koo, Coronary artery axial plaque stress and its relationship with lesion geometry: application of computational fluid dynamics to coronary CT angiography, JACC Cardiovasc. Imaging 8 (2015) 1156–1166.
[8] I. Cicha, A. Wörner, K. Urschel, K. Beronov, M. Goppelt-Struebe, E. Verhoeven, W. G. Daniel, C.D. Garlichs, Carotid Plaque Vulnerability A Positive Feedback between Hemodynamic and Biochemical Mechanisms, 2011, https://doi.org/10.1161/STROKEAHA.111.627265/-/DC1.
[9] L.J. Coward, R.L. Featherstone, M.M. Brown, Safety and Efficacy of Endovascular Treatment of Carotid Artery Stenosis Compared with Carotid Endarterectomy: A Cochrane Systematic Review of the Randomized Evidence, 2005.
[10] M. Dabagh, P. Vasava, P. Jalali, Effects of severity and location of stenosis on the hemodynamics in human aorta and its branches, Med. Biol. Eng. Comput. 53 (2015) 463–476.
[11] M.E. DeBakey, G.M. Lawrie, D.H. Glaeser, Patterns of atherosclerosis and their surgical significance, Ann. Surg. 201 (1985), 115–31.
[12] V. Filardi, Carotid artery stenosis near a bifurcation investigated by fluid dynamic analyses, Neuroradiol. J. 26 (2013) 439–453.
[13] D. Gallo, D.A. Steinman, U. Morbiducci, Insights into the co-localization of magnitude-based versus direction-based indicators of disturbed shear at the carotid bifurcation, J. Biomech. 49 (2016) 2413–2419.

[14] H. Gharahi, B.A. Zambrano, D.C. Zhu, J.K. DeMarco, S. Baek, Computational fluid dynamic simulation of human carotid artery bifurcation based on anatomy and volumetric blood flow rate measured with magnetic resonance imaging, Int. J. Adv. Eng. Sci. Appl. Math. 8 (2016) 40–60.
[15] L.B. Goldstein, Extracranial Carotid Artery Stenosis, 2003, https://doi.org/10.1161/01.STR.0000097803.90702.31.
[16] P.A. Holme, U. Orvim, M.J. Hamers, N.O. Solum, F.R. Brosstad, R.M. Barstad, K. S. Sakariassen, Shear-induced platelet activation and platelet microparticle formation at blood flow conditions as in arteries with a severe stenosis, Arterioscler. Thromb. Vasc. Biol. 17 (1997) 646–653.
[17] H.S. Hosseini, L.A. Taber, How mechanical forces shape the developing eye, Prog. Biophys. Mol. Biol. 137 (2018) 25–36.
[18] Y. Huang, P. Gloviczki, A.A. Duncan, M. Kalra, G.S. Oderich, R.R. DeMartino, W. S. Harmsen, T.C. Bower, Outcomes after early and delayed carotid endarterectomy in patients with symptomatic carotid artery stenosis, J. Vasc. Surg. 67 (2018) 1110–1119, e1.
[19] S. Kefayati, J.S. Milner, D.W. Holdsworth, T.L. Poepping, In vitro shear stress measurements using particle image velocimetry in a family of carotid artery models: effect of stenosis severity, plaque eccentricity, and ulceration, PLoS One 9 (2014) e98209.
[20] B.J. Kim, K.M. Lee, H.Y. Kim, Y.S. Kim, S.-H. Koh, S.H. Heo, D.-I. Chang, Basilar artery plaque and pontine infarction location and vascular geometry, J. Stroke 20 (2018) 92–98.
[21] V.B. Kolachalama, N.W. Bressloff, P.B. Nair, C.P. Shearman, Predictive haemodynamics in a one-dimensional human carotid artery bifurcation. Part I: application to stent design, IEEE Trans. Biomed. Eng. 54 (2007) 802–812.
[22] V.B. Kolachalama, N.W. Bressloff, P.B. Nair, C.P. Shearman, Predictive haemodynamics in a one-dimensional human carotid artery bifurcation. Part II: application to graft design, IEEE Trans. Biomed. Eng. 55 (2008) 1176–1184.
[23] J. Kweon, D.H. Yang, G.B. Kim, N. Kim, M. Paek, A.F. Stalder, A. Greiser, Y.-H. Kim, Four-dimensional flow MRI for evaluation of post-stenotic turbulent flow in a phantom: comparison with flowmeter and computational fluid dynamics, Eur. Radiol. 26 (2016) 3588–3597.
[24] S.-W. Lee, L. Antiga, D.A. Steinman, Correlations among indicators of disturbed flow at the normal carotid bifurcation, J. Biomech. Eng. 131 (2009) 061013.
[25] X. Leng, B. Zhou, X. Deng, L. Davis, M.A. Sutton, T. Shazly, S.M. Lessner, Determination of viscoelastic properties of human carotid atherosclerotic plaque by inverse boundary value analysis, IOP Conf. Ser. Mater. Sci. Eng. 381 (2018) 012171.
[26] Z.-Y. Li, F.P.P. Tan, G. Soloperto, N.B. Wood, X.Y. Xu, J.H. Gillard, Flow pattern analysis in a highly stenotic patient-specific carotid bifurcation model using a turbulence model, Comput. Methods Biomech. Biomed. Eng. 18 (2015) 1099–1107.
[27] X. Liu, L. Ren, H. Xiong, Z. Gao, P. Xu, W. Huang, H. Zhang, W. Wu, Functional assessment of the stenotic carotid artery by CFD based pressure gradient evaluation, Am J Physiol Hear. Circ Physiol 645– 653 (2016), https://doi.org/10.1152/ajpheart.00888.2015.
[28] Q. Long, X.Y. Xu, B. Ariff, S.A. Thom, A.D. Hughes, A. V Stanton, Reconstruction of blood flow patterns in a human carotid bifurcation: a combined CFD and MRI study, J. Magn. Reson. Imaging 11 (2000) 299–311.
[29] Z. Malota, J. Glowacki, W. Sadowski, M. Kostur, Numerical analysis of the impact of flow rate, heart rate, vessel geometry, and degree of stenosis on coronary hemodynamic indices, BMC Cardiovasc. Disord. 18 (2018) 132.
[30] M. Markl, F. Wegent, T. Zech, S. Bauer, C. Strecker, M. Schumacher, C. Weiller, J. Hennig, A. Harloff, In Vivo Wall Shear Stress Distribution in the Carotid Artery Effect of Bifurcation Geometry, Internal Carotid Artery Stenosis, and Recanalization Therapy, 2010, https://doi.org/10.1161/CIRCIMAGING.110.958504.
[31] I. Marshall, S. Zhao, P. Papathanasopoulou, P. Hoskins, Y. Xu, MRI and CFD studies of pulsatile flow in healthy and stenosed carotid bifurcation models, J. Biomech. 37 (2004) 679–687.
[32] B. Merei, P. Badel, L. Davis, M.A. Sutton, S. Avril, S.M. Lessner, Atherosclerotic plaque delamination: experiments and 2D finite element model to simulate plaque peeling in two strains of transgenic mice, J. Mech. Behav. Biomed. Mater. 67 (2017) 19–30.
[33] D.R. Morris, K. Ayabe, T. Inoue, N. Sakai, R. Bulbulia, A. Halliday, S. Goto, Evidence-based carotid interventions for stroke prevention: state-of-the-art review, J. Atheroscler. Thromb. 24 (2017) 373–387.
[34] A.R. Naylor, Z. Mehta, P.M. Rothwell, P.R.F. Bell, Carotid artery disease and stroke during coronary artery bypass: a critical review of the literature, Eur. J. Vasc. Endovasc. Surg. 23 (2002) 283–294.
[35] R. Pokras, M.L. Dyken, Dramatic changes in the performance of endarterectomy for diseases of the extracranial arteries of the head, Stroke 19 (1988), 1289–90.
[36] D.A. Prim, M.A. Mohamed, B.A. Lane, K. Poblete, M.A. Wierzbicki, S.M. Lessner, T. Shazly, J.F. Eberth, Comparative biaxial mechanics of mammalian carotid arteries, PLoS One 1–19 (2018).
[37] J.J. Ricotta, A. AbuRahma, E. Ascher, M. Eskandari, P. Faries, B.K. Lal, Updated Society for Vascular Surgery guidelines for management of extracranial carotid disease: executive summary, J. Vasc. Surg. 54 (2011) 832–836.
[38] C.M. Schirmer, A.M. Malek, Computational fluid dynamic characterization of carotid bifurcation stenosis in patient-based geometries, Brain Behav 2 (2012) 42–52.
[39] A. Shahidian, A.G. Hassankiadeh, Stress analysis of internal carotid artery with low stenosis level: the effect of material model and plaque geometry, J. Mech. Med. Biol. 17 (2017) 1750098.
[40] M. Sharzehee, S.S. Khalafvand, H.-C. Han, Fluid-structure interaction modeling of aneurysmal arteries under steady-state and pulsatile blood flow: a stability analysis, Comput. Methods Biomech. Biomed. Eng. 21 (2018) 219–231.
[41] J.S. Stroud, S.A. Berger, D. Saloner, Numerical analysis of flow through a severely stenotic carotid artery bifurcation, J. Biomech. Eng. 124 (9) (2002).
[42] B. Su, Y. Huo, G.S. Kassab, F. Kabinejadian, S. Kim, H.L. Leo, L. Zhong, Numerical investigation of blood flow in three-dimensional porcine left anterior descending artery with various stenoses, Comput. Biol. Med. 47 (2014) 130–138.
[43] F.P.P. Tan, G. Soloperto, S. Bashford, N.B. Wood, S. Thom, A. Hughes, X.Y. Xu, Analysis of flow disturbance in a stenosed carotid artery bifurcation using two-equation transitional and turbulence models, J. Biomech. Eng. 130 (2008) 061008.
[44] F.-B. Tian, L. Zhu, P.-W. Fok, X.-Y. Lu, Simulation of a pulsatile non-Newtonian flow past a stenosed 2D artery with atherosclerosis, Comput. Biol. Med. 43 (2013) 1098–1113.
[45] I.E. Vignon-Clementel, C.A. Figueroa, K.E. Jansen, C.A. Taylor, Outflow boundary conditions for 3D simulations of non-periodic blood flow and pressure fields in deformable arteries, Comput. Methods Biomech. Biomed. Eng. 13 (2010) 625–640.
[46] P. Xu, X. Liu, H. Zhang, D. Ghista, D. Zhang, C. Shi, W. Huang, Assessment of boundary conditions for CFD simulation in human carotid artery, Biomechanics Model. Mechanobiol. (2018), https://doi.org/10.1007/s10237-018-1045-4.
[47] C.K. Zarins, D.P. Giddens, B.K. Bharadvaj, V.S. Sottiurai, R.F. Mabon, S. Glagov, Carotid bifurcation atherosclerosis. Quantitative correlation of plaque localization with flow velocity profiles and wall shear stress, Circ. Res. 53 (1983), 502–14.
[48] S. Zhao, B. Ariff, Q. Long, A. Hughes, S. Thom, A. Stanton, X. Xu, Inter-individual variations in wall shear stress and mechanical stress distributions at the carotid artery bifurcation of healthy humans, J. Biomech. 35 (2002) 1367–1377.